

## Observation of three-dimensional photonic Dirac points and spin-polarized surface arcs

Guo, Qinghua; You, Oubo; Yang, Biao; Sellman, James B.; Blythe, Edward; Liu, Hongchao; Xiang, Yuanjiang; Li, Jensen; Fan, Dianyuan; Chen, Jing; Chan, C. T.; Zhang, Shuang

DOI:

[10.1103/PhysRevLett.122.203903](https://doi.org/10.1103/PhysRevLett.122.203903)

[10.1103/PhysRevLett.122.203903](https://doi.org/10.1103/PhysRevLett.122.203903)

License:

None: All rights reserved

*Document Version*

Publisher's PDF, also known as Version of record

*Citation for published version (Harvard):*

Guo, Q, You, O, Yang, B, Sellman, JB, Blythe, E, Liu, H, Xiang, Y, Li, J, Fan, D, Chen, J, Chan, CT & Zhang, S 2019, 'Observation of three-dimensional photonic Dirac points and spin-polarized surface arcs', *Physical Review Letters*, vol. 122, no. 20, 203903. <https://doi.org/10.1103/PhysRevLett.122.203903>, <https://doi.org/10.1103/PhysRevLett.122.203903>

[Link to publication on Research at Birmingham portal](#)

### **Publisher Rights Statement:**

Checked for eligibility: 19/06/2019

Guo, Q., You, O., Yang, B., Sellman, J.B., Blythe, E., Liu, H., Xiang, Y., Li, J., Fan, D., Chen, J. and Chan, C.T., 2019. Observation of three-dimensional photonic Dirac points and spin-polarized surface arcs. *Physical review letters*, 122(20), p.203903. © 2019 American Physical Society. <https://doi.org/10.1103/PhysRevLett.122.203903>

### **General rights**

Unless a licence is specified above, all rights (including copyright and moral rights) in this document are retained by the authors and/or the copyright holders. The express permission of the copyright holder must be obtained for any use of this material other than for purposes permitted by law.

- Users may freely distribute the URL that is used to identify this publication.
- Users may download and/or print one copy of the publication from the University of Birmingham research portal for the purpose of private study or non-commercial research.
- User may use extracts from the document in line with the concept of 'fair dealing' under the Copyright, Designs and Patents Act 1988 (?)
- Users may not further distribute the material nor use it for the purposes of commercial gain.

Where a licence is displayed above, please note the terms and conditions of the licence govern your use of this document.

When citing, please reference the published version.

### **Take down policy**

While the University of Birmingham exercises care and attention in making items available there are rare occasions when an item has been uploaded in error or has been deemed to be commercially or otherwise sensitive.

If you believe that this is the case for this document, please contact [UBIRA@lists.bham.ac.uk](mailto:UBIRA@lists.bham.ac.uk) providing details and we will remove access to the work immediately and investigate.

## Observation of Three-Dimensional Photonic Dirac Points and Spin-Polarized Surface Arcs

Qinghua Guo,<sup>1,2,\*</sup> Oubo You,<sup>1,3,\*</sup> Biao Yang,<sup>1,4,\*</sup> James B. Sellman,<sup>1</sup> Edward Blythe,<sup>1</sup> Hongchao Liu,<sup>1</sup> Yuanjiang Xiang,<sup>3</sup> Jensen Li,<sup>1,2</sup> Dianyuan Fan,<sup>3</sup> Jing Chen,<sup>5,†</sup> C. T. Chan,<sup>2,‡</sup> and Shuang Zhang<sup>1,§</sup>

<sup>1</sup>*School of Physics & Astronomy, University of Birmingham, Birmingham, B15 2TT, United Kingdom*

<sup>2</sup>*Department of Physics and Center for Metamaterials Research,*

*The Hong Kong University of Science and Technology, Hong Kong, China*

<sup>3</sup>*International Collaborative Laboratory of 2D Materials for Optoelectronic Science and Technology of Ministry of Education, Shenzhen University, Shenzhen 518060, China*

<sup>4</sup>*College of Advanced Interdisciplinary Studies, National University of Defense Technology, Changsha 410073, China*

<sup>5</sup>*School of Physics, Nankai University, Tianjin 300071, China*



(Received 27 November 2018; published 24 May 2019)

Three-dimensional (3D) Dirac points inheriting relativistic effects from high-energy physics appear as gapless excitations in the topological band theory. Hosting fourfold linear dispersion, they play the central role among various topological phases, such as representing the degeneracy of paired Weyl nodes carrying opposite chiralities. While they have been extensively investigated in solid state systems for electrons, 3D Dirac points have not yet been observed in any classical systems. Here, we experimentally demonstrate 3D photonic Dirac points in the microwave region with an elaborately designed metamaterial, where two symmetrically placed Dirac points are stabilized by electromagnetic duality symmetry. Furthermore, spin-polarized surface arcs (counterparts of Fermi arcs in electronic systems) are demonstrated, which opens the gate toward implementing spin-multiplexed topological surface wave propagation. Closely linked to other exotic states through topological phase transitions, our system offers an effective medium platform for topological photonics.

DOI: [10.1103/PhysRevLett.122.203903](https://doi.org/10.1103/PhysRevLett.122.203903)

Topological phases arise from the elegant mathematical structures imposed by the interplay between symmetry and topology, and the recent study of band topology has produced many interesting surface transport phenomena, such as unidirectional propagation of surface waves and related relativistic behaviors [1–6]. Graphene, as one of the most well-known examples, consisting of a monolayer of two-dimensional honeycomb lattice of carbon atoms, has the band structure that exhibits linear crossings at discrete locations in the momentum space, which are known as Dirac points. The quasiparticles around Dirac points are massless, leading to many fascinating quantum mechanical observations such as chiral tunneling and the Klein paradox [7]. Weyl points are counterparts of Dirac points in three-dimensional systems, and Weyl fermion is the solution to the three-dimensional massless Dirac equation. Different from those accidental or symmetry protected double degeneracies, Weyl points are robustly protected by the underlying topology. Each Weyl point as source or sink of Berry flux behaves as a magnetic monopole in the momentum space. Because of Nielsen-Ninomiya no-go theorem [8,9], Weyl points are only ever found in pairs of opposite charges. Three-dimensional (3D) Dirac points [10,11] are the crossings of the linear energy dispersion curves with fourfold degeneracy, which are

equivalent to overlapping of two Weyl points with opposite topological charges in the momentum space.

With the net Chern number being zero, the 3D Dirac point is not topologically protected. Usually, extra constraints are required to stabilize the fourfold degeneracy, such as spatial group symmetries [10–14], where the Dirac state space is constructed by spatial Bloch modes. In the spinful electronic systems, twofold spin degeneracy can be guaranteed at time-reversal invariant momenta due to Kramers theorem, and crystalline symmetries are required to enforce extra double degeneracy in the orbital subspace. For other spinless cases, including photonics and acoustic or mechanics, one needs to introduce nonsymmorphic space groups to realize four-dimensional irreducible representation on the Brillouin zone boundary [4,15,16], and hence 3D Dirac points. When external symmetry-breaking terms are introduced, they may split into Weyl points or become gapped as topological insulators [4]. Therefore, this 3D Dirac semimetal [10,17] lies at the topological phase transition point between various topological phases. It shares multiple exotic topological features with other topological materials, such as Fermi arcs and chiral anomaly with Weyl semimetals [18,19], and spin-dependent surface states with topological insulators [20,21]. Despite the important role they play in topological

physics, no experimental observation of 3D Dirac points has been reported in any classical systems so far.

Here, we construct 3D photonic Dirac points by further imposing the electromagnetic duality symmetry [22], which represents an internal symmetry of the electromagnetic field [23]. When the wavelength of electromagnetic waves approaches the long wavelength limit, effective medium theory can be employed to describe the optical properties of the structured media [24–26], which has been used to the topological metamaterials [27–30]. In particular, Weyl points can be realized in metamaterials by the crossing between a longitudinal mode and a circularly polarized transverse mode, where the Weyl point charge is inherited from the spin of the circular transverse mode [29–32]. It has been shown that the intrinsic polarization states can also be used to construct the Dirac state space in judiciously designed photonic metamaterials for realizing 3D Dirac

degeneracies [22]. In artificial metamaterials, duality symmetry requires the proportionality between permittivity and permeability tensors, such as  $\vec{\epsilon} = \eta \vec{\mu}$  ( $\eta > 0$ ). Compared with a single Weyl point, it is spanned by two longitudinal modes and two circularly polarized transverse modes as discussed in the reference [22], the fourfold band crossing between the two degenerate transverse modes and the two degenerate longitudinal modes is guaranteed by the orthogonality between them. It is expected that spin-polarized topological surface states exist at the interface between air and the Dirac metamaterials.

In order to simultaneously realize the electric and magnetic longitudinal modes, we utilize metallic helical elements to introduce both electric and magnetic resonances in the  $z$  direction, as shown in Fig. 1(a). Meanwhile, in order to eliminate the unwanted overall chirality of the metamaterial, each unit cell consists of two layers of helical

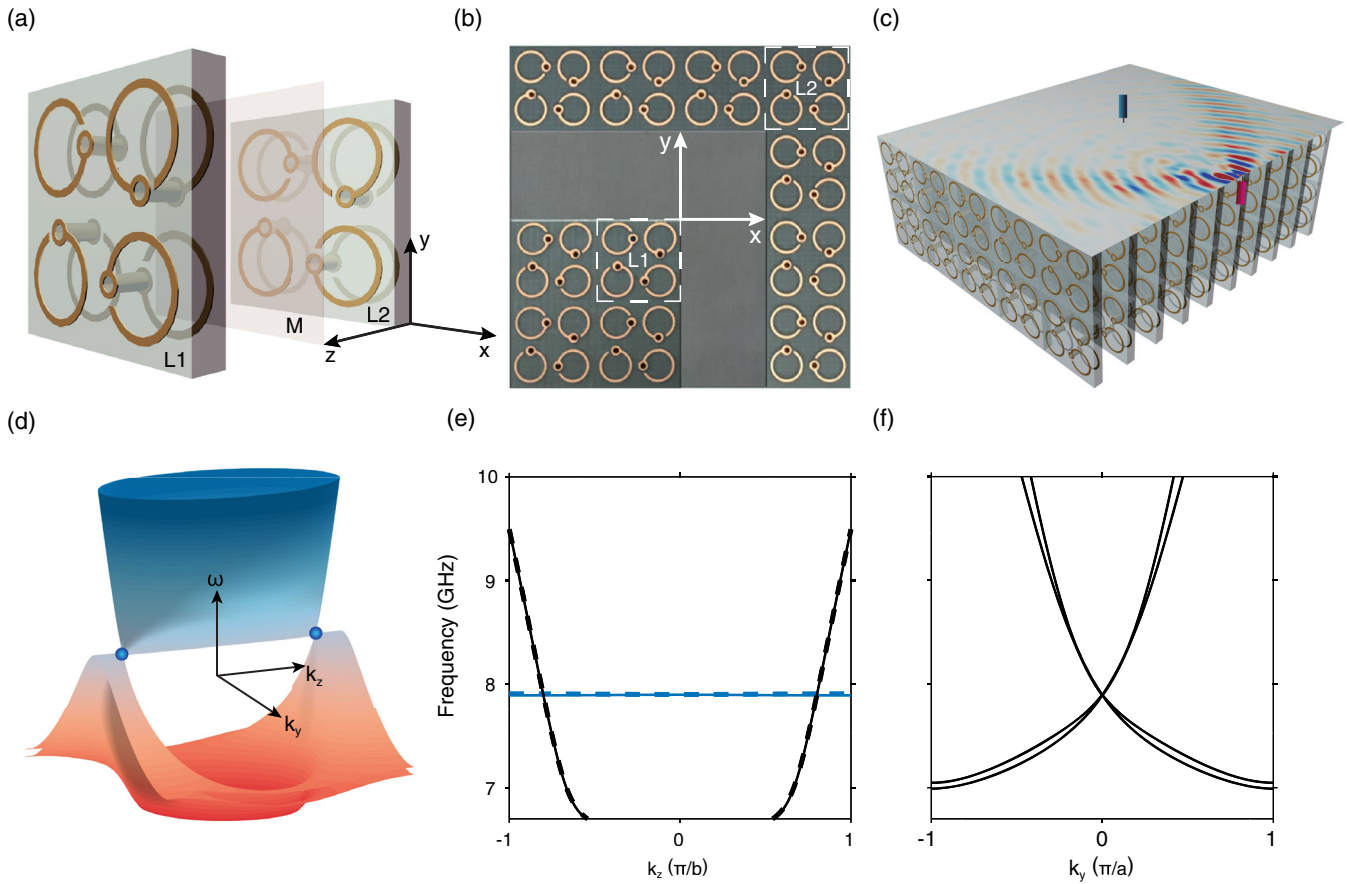


FIG. 1. Design of three-dimensional photonic Dirac metamaterial. (a) Schematic of the metamaterial structure. Each unit cell consists of eight helical elements. Along the  $z$  direction, there are two sets of helical elements related by mirror symmetry indicated by  $M$  (four left-handed and four right-handed helical elements). In the  $x$ - $y$  plane, the unit cell possesses  $C_4$  rotation symmetry along  $z$  to ensure the degeneracy between the two circularly polarized transverse states. (b) Sample fabricated with printed circuit board technology. The helical elements are etched in the 1-mm-thick hosting material (dielectric constant of 2.2). Between two structured layers there is a 3-mm-thick spacer with the same dielectric constant. The in-plane period (marked as the white dashed squares) is  $6.8 \times 6.8 \text{ mm}^2$ . The period along  $z$  is 8 mm. (c) Sample configuration for the experimental measurement. The sample is stacked layer by layer to form a three-dimensional bulk metamaterial. In the measurement, two antennas are used, with one working as the source (magenta) and the other working as probe (cyan). (d) The full wave simulation shows the presence of two fourfold degenerate Dirac points at the same frequency around 7.92 GHz. (e) The simulated dispersion along the  $k_z$  directions around the Dirac points. (f) Similar to (e) but along  $k_y$ .

elements with opposite chiralities: the four identical helical elements [33] on layer 1 ( $L1$ ) possessing left-handed chirality, while those on layer 2 ( $L2$ ) have right-handed chirality. They are related to each other through the mirror operation as indicated by plane  $M$ . Finely tuning the structure parameters of the helical elements leads to double degeneracy of the two longitudinal modes. Finally, the helical elements are arranged to preserve  $C_4$  rotation symmetry in the  $x$ - $y$  plane to ensure the in-plane isotropic response, and thus guaranteeing degeneracy between the two circularly polarized transverse modes propagating along the  $z$  direction as well. In total, each unit cell consists of eight helical elements and possesses inversion symmetry.

As shown by the simulated band structure (calculated using CST MICROWAVE STUDIO) in Fig. 1(d), two Dirac points (marked by the blue spheres) are symmetrically located on the  $k_z$  axis at the same frequency around 7.92 GHz. Because of the flat dispersion of the longitudinal modes, the tilted Dirac points lie right at the transition between type I and type II Dirac points [31], and they are therefore called transitional Dirac points here. To clearly see the massless dispersion around the Dirac points, Figs. 1(e) and 1(f) show the bands linearly threading through the Dirac points along  $k_z$  and  $k_x(k_y)$ , respectively. Along the  $k_z$  direction, the two longitudinal modes (blue solid and dashed lines) and the two transverse modes (black solid and dashed lines) are degenerate across the entire frequency range. However, the degeneracy is slightly lifted along the  $k_y$  direction away from the Dirac point, because the condition for ideal electromagnetic duality, i.e., exactly tensor matching between permittivity and permeability, cannot exist in a wide frequency range [27] (Fig. S1, [34]).

The sample is fabricated using the Printed Circuit Board technology. The left- or right-handed helical elements are printed on a 1-mm-thick dielectric layer (with a dielectric constant of 2.2) as shown in Fig. 1(b). Between them, a spacer layer with a thickness of 3 mm and a dielectric constant of 2.2 is placed to prevent short contacting between neighbor metallic elements. Finally, a 3D bulk metamaterial is constructed through layer stacking (70 periods) along the  $z$  direction as schematically shown in Fig. 1(c) with each period (8 mm) consisting of a  $L1$ -spacer- $L2$ -spacer configuration. For each structured layer, there are 20 and 70 unit cells with an identical period  $a = 6.8$  mm along  $x$  and  $y$ , respectively. The realistic sample is shown in Fig. S2 [34].

We probe the bulk states of the metamaterials using a transmission method, in which the bulk states could be enhanced compared to the surface state. One antenna is placed at the center of the bottom surface of the sample as a source, and another probe antenna raster scans the transmitted field on the top surface. After subsequent Fourier transformations, we obtain the projection of the bulk states

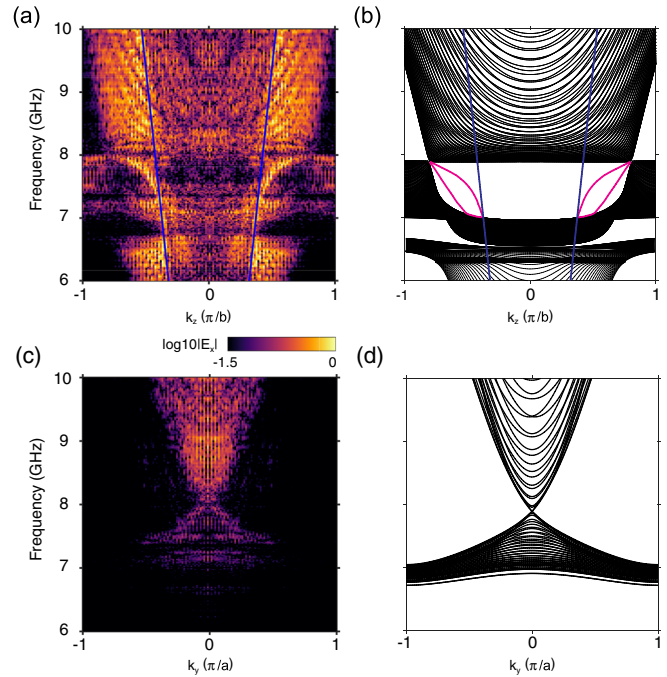


FIG. 2. Observation of three-dimensional photonic Dirac points. (a),(c) Experimentally mapped band projection around the Dirac point along the  $k_z$  and  $k_y$  direction, respectively. (b), (d) The corresponding simulation results from CST MICROWAVE STUDIO. Blue and magenta lines indicate light cone and surface states, respectively.

on the  $k_y$ - $k_z$  plane. The projected band spectra along the  $k_z$  and  $k_y$  directions are shown in Figs. 2(a) and 2(c), respectively. The 3D Dirac points are observed around frequency 7.92 GHz. Figures 2(b) and 2(d) show the corresponding simulated results for reference, where linear dispersion along different directions confirms the presence of the photonic Dirac points. Besides the bulk states, one of the surface states is clearly observed as the bright line connecting between the Dirac points and light cone (blue line) as shown in Fig. 2(a). The simulation [Fig. 2(b)] shows two surface states; however, the other one is hard to discern from the measurement results. As expected, away from the Dirac point the projected bulk states are gapped, which agrees well with the simulation results shown in Fig. S3 [34].

Surface state arcs, corresponding to Fermi arcs in electronic systems, are important topological signatures of Dirac points. In order to clearly measure the surface state arcs, we use a slightly different experimental configuration as shown in Fig. 1(c): the source antenna is moved to the edge of the top surface for better excitation of surface waves. The spatial field in Fig. 1(c) shows the propagating electromagnetic wave measured in this configuration. Compared with the simulated bulk and surface states distribution in Figs. 3(d)–3(f), the surface state arcs could be clearly distinguished and observed at frequencies 7.8, 7.92, and 8.1 GHz, respectively, as shown in Figs. 3(a)–3(c).

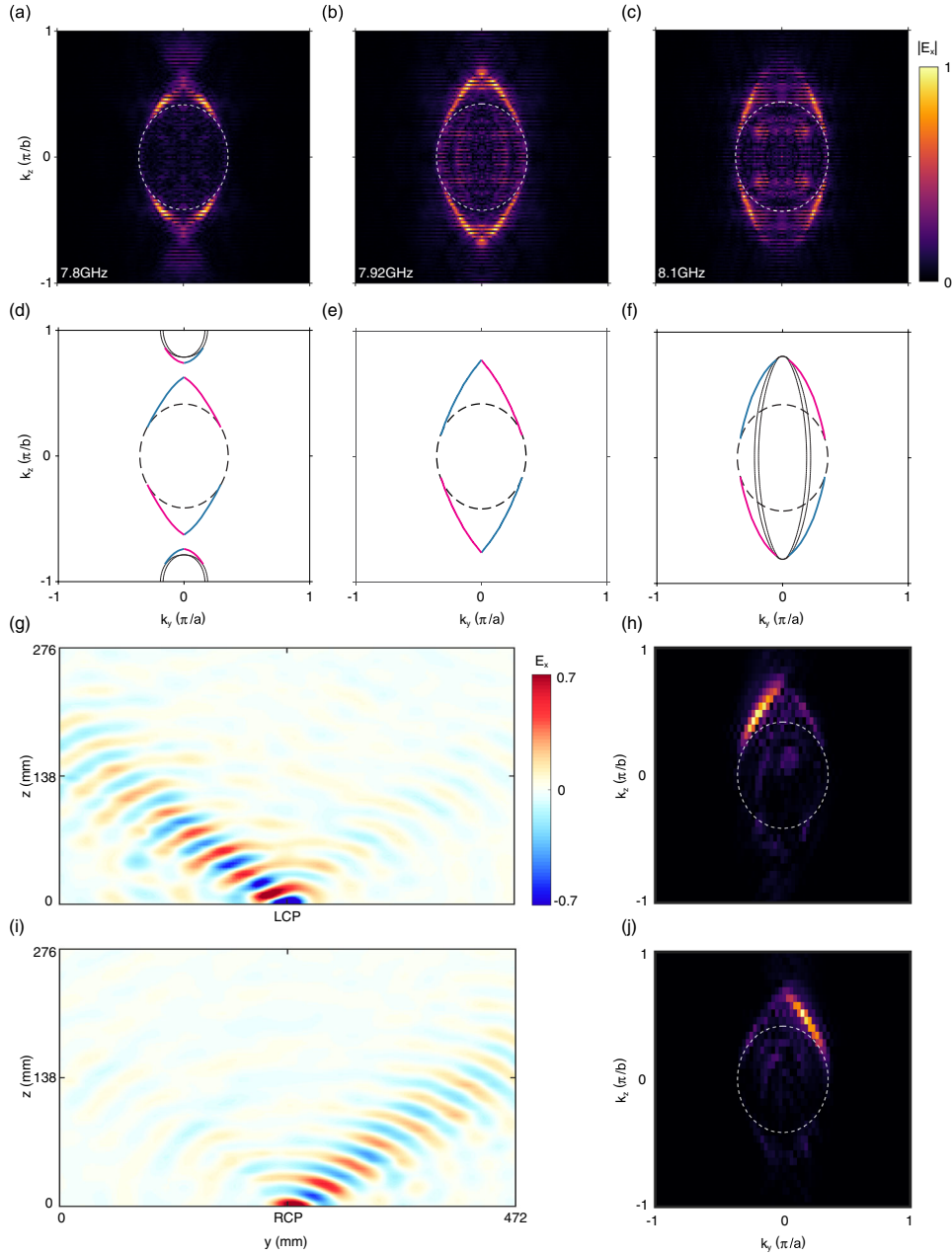


FIG. 3. Spin-polarized photonic surface arcs and surface waves. (a)–(c) Experimentally measured surface state arcs at the frequency 7.8 GHz (below Dirac point), 7.92 GHz (at Dirac point), and 8.1 GHz (above Dirac point), respectively. (d)–(f) The corresponding simulated bulk and surface states, where cyan and magenta curves indicate opposite spinful surface states from CST MICROWAVE STUDIO. Black solid lines indicate simulated bulk states. (g) Measured real space surface wave propagation excited by left circular polarization. (h) Spin-polarized surface states in momentum space after Fourier transformation from (g). (i),(j) Similar to (g),(h) but excited by right circular polarization. In each panel, the dashed circle indicates the light cone.

They correspond to the frequency below, at, and above the Dirac points.

At the Dirac point, two Fermi arcs emerge from the Dirac point and tangentially terminate at the light cone. Since a Dirac point consists of two Weyl points with opposite charges, each Fermi arc from the corresponding Weyl point should be spin polarized, as distinguished by the magenta and cyan colors in Figs. 3(d)–3(f). Further, effective media

analysis [22] shows that the two Fermi arcs exhibit left (right) circular polarization [LCP (RCP)] with the plane of the polarization being parallel to the Fermi arcs. In order to verify the spin-dependent nature of the Fermi arc, we further use circularly polarized antennas to selectively excite each spin-polarized surface state arc. As shown in Figs. 3(g) and 3(i), under LCP (RCP) excitation, the surface waves are tilted towards the  $-/+y$  direction. The

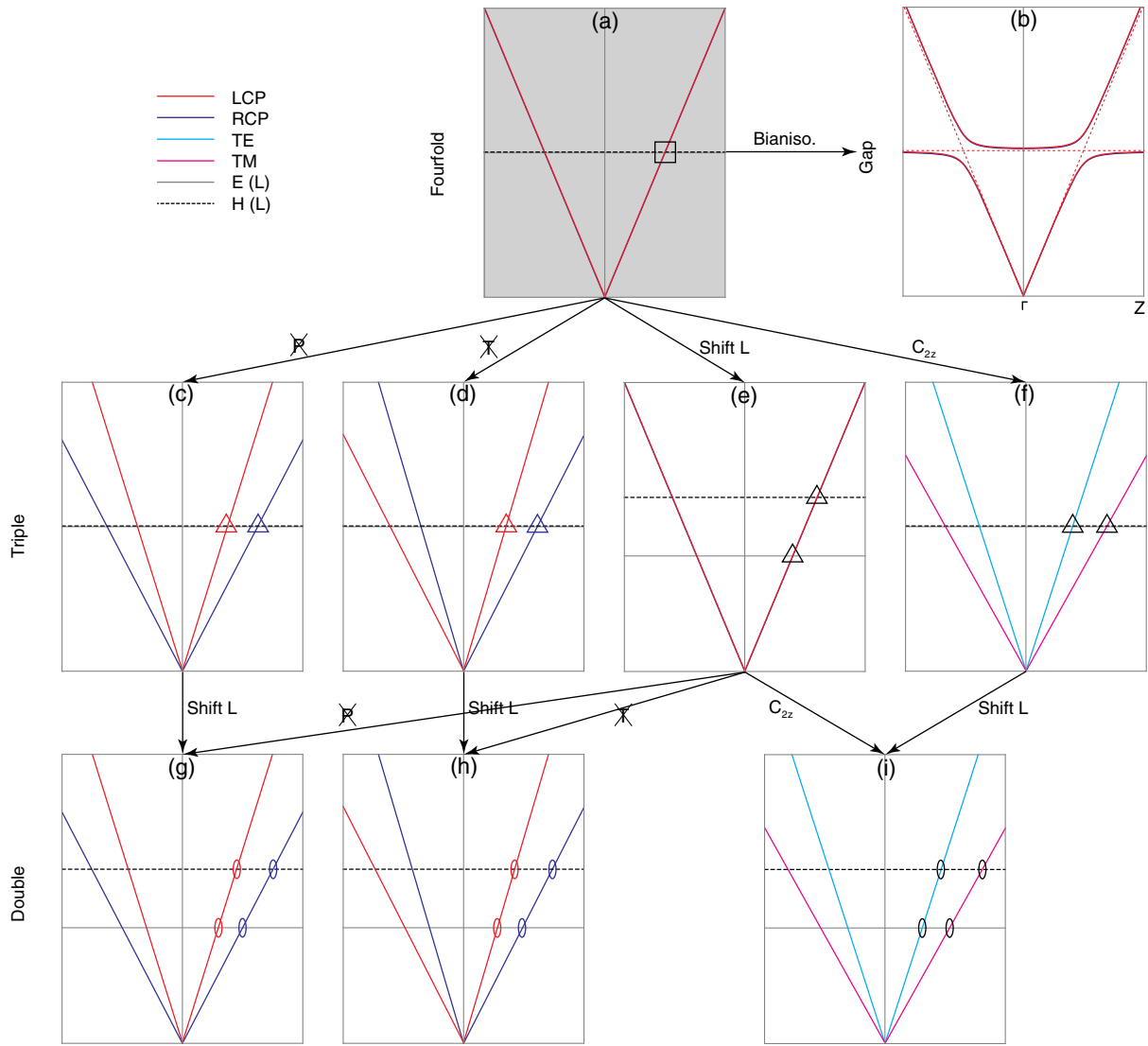


FIG. 4. Illustration of the photonic topological phase transition on the metamaterial (effective medium) platform. Adding a bianisotropic term in the  $y$ - $z$  plane transforms the Dirac metamaterial (a) into a photonic topological insulator (b), where red dashed lines indicate gapless interface states across the gap. Breaking either inversion symmetry  $P$  or time-reversal symmetry  $T$  splits the Dirac points (a) into two transient phases (c) and (d), where each triple degenerate point (TDP) consists of two longitudinal modes and one circularly polarized transverse mode. After shifting the two longitudinal modes (shift  $L$ ) away from each other, (c) and (d) transform into (g) and (h), respectively. The TDPs in (e) and (f) are topologically neutral. By maintaining only the  $C_2$  rotational symmetry along the  $z$  direction, i.e., breaking the  $C_4$  rotational symmetry in (e), or breaking the degeneracy of the two longitudinal modes in (f), they can transform into nodal lines (i). Hollow square, triangle, and ellipsoid represent fourfold, triple, and double degeneracy, respectively. Colorful (black) symbols indicate chiral (neutral) gapless excitations. The gray- (black)-dashed, red (blue), and cyan (magenta) lines indicate mutually orthogonal: electric- (magnetic)-longitudinal [ $E(L)$ / $H(L)$ ], left (right) circularly polarized [LCP (RCP)] transverse- and linear-polarized [TE (TM)] transverse modes, respectively. Corresponding hypothetical constitutive relation examples for panels (a)–(i) are given in Table S1.

asymmetry clearly demonstrates the spin-momentum locking property of the surface state arcs [Figs. 3(h) and 3(j)] in the Dirac system. Furthermore, the 3D views of spin-dependent surface wave propagation are shown in Fig. S4 [34], where they bypass the rectangle hinges with little backscattering [22]. The spin-resolved intensity of the surface state arcs at different frequencies is presented in Fig. S5 [34]. The launching and propagation of robust

spin-momentum locked surface wave demonstrated here may pave a new way in information processing, such as spin-multiplexed channels.

Below the Dirac frequency, the equipfrequency contours of the bulk states [black solid lines in Fig. 3(d)] form two almost-overlapping hyperboloids (more experimental results are shown in Fig. S6 [34]). As shown in Figs. 3(a) and 3(d), the surface states still exist at the gap between the

metamaterial bulk state and light cone. However, there is a small gap between the surface state as numerically shown in Fig. 3(d), where the impedance mismatch between metamaterial and air mixes the LCP and RCP surface states, leading to anticrossing between the two surface state arcs. Above the Dirac points [Figs. 3(c) and 3(f)], the equifrequency contours of the surface states show strong resemblance to the famous Dyakonov surface waves in anisotropic crystals [35].

As a gapless topological phase, Dirac semimetal can be viewed as a parent topological phase which can generate various interesting topological materials, e.g., topological insulators, Weyl semimetals, and nodal lines, through symmetry reduction. Based on electromagnetic effective media theory, here we show the hierarchy structure of topological phase transitions. We define Hermitian constitutive tensor for the effective media as  $\vec{D} = \vec{\epsilon} \vec{E} + i\vec{\gamma} \vec{H}$  and  $\vec{B} = \vec{\mu} \vec{H} - i\vec{\gamma}' \vec{E}$ , where  $\vec{\gamma}$  indicates the electromagnetic coupling matrix. For each topological phase we discuss in the following, these corresponding constitutive tensors are explicitly presented in Table S1 [34]. We start from the 3D Dirac points [Fig. 4(a)] and assume  $\vec{\epsilon} = \vec{\mu} = \text{diag}[1, 1, 1 - (\omega_p^2/\omega^2)]$  with  $\omega_p$  being the plasma frequency [Table S1(a)] [34]. First, by introducing a bianisotropic term [13,14,27,34] into the  $y$ - $z$  plane ( $\vec{\gamma}_{zy} = -\vec{\gamma}_{yz} \neq 0$ ), the Dirac point is gapped and the material transforms to a photonic topological insulator as shown in Fig. 4(b), where gapless interface states (red dashed lines) exist across the bulk gap. When breaking either inversion ( $\vec{\gamma}_{xx/yy} \neq 0$ ) [28,29,34] or time-reversal ( $\vec{\epsilon}_{xy} = -\vec{\epsilon}_{yx} \neq 0$ ) [31,34,36] symmetry and lifting the degeneracy of the two longitudinal modes, the Dirac point splits into four Weyl points as shown in Figs. 4(g) and 4(h). Each Weyl state space is spanned by one electric (magnetic) longitudinal mode and one LCP (RCP). When the crossing is formed by two orthogonal linear-polarized longitudinal or transverse modes ( $\vec{\epsilon}_{ij} = \vec{\mu}_{ij} = 0$ ,  $\vec{\gamma} = 0$ ,  $i \neq j$ ) as shown in Fig. 4(i), one can realize topological nodal lines [37]. Finally, several triply degenerate points (TDPs) appear as transient phases as shown in Figs. 4(c)–4(f). Among them, the TDPs in Figs. 4(c) and 4(d) consisting of two spinless longitudinal modes and one spinful circularly polarized transverse mode are chiral and represent nontrivial triple gapless states [38,39]. In Fig. 4(e), the state space of TDPs is constructed by one longitudinal mode and two degenerate circularly polarized transverse modes, which are topologically neutral and behave as triply degenerate Dirac points. They can further split into Weyl points by breaking either inversion or time-reversal symmetry [Figs. 4(g) and 4(h)] as well. Neutral TDPs can also be formed by two longitudinal modes and one linear-polarized transverse mode [transverse electric (transverse magnetic), TE (TM)], as shown in Fig. 4(f).

In summary, we have experimentally demonstrated 3D Dirac degeneracies in a photonic metamaterial operating at microwave frequencies. The presence of 3D Dirac points has been confirmed by demonstrating both the bulk states and the spin-polarized surface state arcs. The demonstrated Dirac degeneracies provide a platform for studying the transition between variously different photonic topological states. Moreover, our demonstrated surface state spin-orbit coupling shows great potential in manipulating topological surface photonics. The slightly gapped surface states may also lead to observation of surface Zitterbewegung oscillation [40]. With introducing extra strain to the Dirac metamaterials, Landau quantization and quasiparticle interference could be observed [41,42]. Our structure consists of metallic helical elements, which are usually very lossy at optical frequency. However, it works at terahertz and even far-infrared bands provided, and the structure can be readily fabricated using three-dimensional laser writing technologies [43–45].

This work was financially supported by the European Research Council Consolidator Grant (Topological), Horizon 2020 Action Project Grant No. 734578 (D-SPA), Leverhulme Trust (Grant No. RPG-2012-674) and Research Grants Council Hong Kong (16304717, AoE/P-02/12). Q.G. acknowledges the financial support of the National Natural Science Foundation of China (Grant No. 11604216). S.Z. acknowledges support from the Royal Society and Wolfson Foundation. J.C. acknowledges the financial support National Natural Science Foundation of China (Grants No. 11574162 and No. 11874228).

\*These authors contributed equally to this work.

†Corresponding author.

jchen4@nankai.edu.cn

‡Corresponding author.

phchan@ust.hk

§Corresponding author.

s.zhang@bham.ac.uk

- [1] M. Z. Hasan and C. L. Kane, *Rev. Mod. Phys.* **82**, 3045 (2010).
- [2] X.-L. Qi and S.-C. Zhang, *Rev. Mod. Phys.* **83**, 1057 (2011).
- [3] C.-K. Chiu, J. C. Y. Teo, A. P. Schnyder, and S. Ryu, *Rev. Mod. Phys.* **88**, 035005 (2016).
- [4] N. P. Armitage, E. J. Mele, and A. Vishwanath, *Rev. Mod. Phys.* **90**, 015001 (2018).
- [5] T. Ozawa *et al.*, *Rev. Mod. Phys.* **91**, 015006 (2019).
- [6] G. E. Volovik, *Phys. Usp.* **61**, 89 (2018).
- [7] M. I. Katsnelson, K. S. Novoselov, and A. K. Geim, *Nat. Phys.* **2**, 620 (2006).
- [8] H. B. Nielsen and M. Ninomiya, *Nucl. Phys.* **B185**, 20 (1981).
- [9] H. B. Nielsen and M. Ninomiya, *Nucl. Phys.* **B193**, 173 (1981).
- [10] S. M. Young, S. Zaheer, J. C. Y. Teo, C. L. Kane, E. J. Mele, and A. M. Rappe, *Phys. Rev. Lett.* **108**, 140405 (2012).

- [11] H. X. Wang, L. Xu, H. Y. Chen, and J.-H. Jiang, *Phys. Rev. B* **93**, 235155 (2016).
- [12] B.-J. Yang and N. Nagaosa, *Nat. Commun.* **5**, 4898 (2014).
- [13] A. Slobozhanyuk, S. H. Mousavi, X. Ni, D. Smirnova, Y. S. Kivshar, and A. B. Khanikaev, *Nat. Photonics* **11**, 130 (2017).
- [14] Y. Yang, Z. Gao, H. Xue, L. Zhang, M. He, Z. Yang, R. Singh, Y. Chong, B. Zhang, and H. Chen, *Nature (London)* **565**, 622 (2019).
- [15] L. Lu, C. Fang, L. Fu, S. G. Johnson, J. D. Joannopoulos, and M. Soljačić, *Nat. Phys.* **12**, 337 (2016).
- [16] H.-X. Wang, Y. Chen, Z. H. Hang, H.-Y. Kee, and J.-H. Jiang, *npj Quantum Mater.* **2**, 54 (2017).
- [17] Z. K. Liu *et al.*, *Science* **343**, 864 (2014).
- [18] J. Xiong, S. K. Kushwaha, T. Liang, J. W. Krizan, M. Hirschberger, W. Wang, R. J. Cava, and N. P. Ong, *Science* **350**, 413 (2015).
- [19] A. C. Potter, I. Kimchi, and A. Vishwanath, *Nat. Commun.* **5**, 5161 (2014).
- [20] S.-Y. Xu *et al.*, *Science* **347**, 294 (2015).
- [21] D. Hsieh *et al.*, *Nature (London)* **460**, 1101 (2009).
- [22] Q. Guo, B. Yang, L. Xia, W. Gao, H. Liu, J. Chen, Y. Xiang, and S. Zhang, *Phys. Rev. Lett.* **119**, 213901 (2017).
- [23] I. Fernandez-Corbaton, X. Zambrana-Puyalto, N. Tischler, X. Vidal, M. L. Juan, and G. Molina-Terriza, *Phys. Rev. Lett.* **111**, 060401 (2013).
- [24] N. Engheta and R. W. Ziolkowski, *Metamaterials: Physics and Engineering Explorations* (John Wiley & Sons & IEEE Press, New York, 2006).
- [25] W. Cai and V. Shalaev, *Optical Metamaterials: Fundamentals and Applications* (Springer International Publishing, New York, 2009).
- [26] Y. Liu and X. Zhang, *Chem. Soc. Rev.* **40**, 2494 (2011).
- [27] A. B. Khanikaev, S. Hossein Mousavi, W.-K. Tse, M. Kargarian, A. H. MacDonald, and G. Shvets, *Nat. Mater.* **12**, 233 (2013).
- [28] W. Gao, M. Lawrence, B. Yang, F. Liu, F. Fang, B. Béri, J. Li, and S. Zhang, *Phys. Rev. Lett.* **114**, 037402 (2015).
- [29] B. Yang *et al.*, *Nat. Commun.* **8**, 97 (2017).
- [30] M. Xiao, Q. Lin, and S. Fan, *Phys. Rev. Lett.* **117**, 057401 (2016).
- [31] W. Gao, B. Yang, M. Lawrence, F. Fang, B. Béri, and S. Zhang, *Nat. Commun.* **7**, 12435 (2016).
- [32] B. Yang *et al.*, *Science* **359**, 1013 (2018).
- [33] B. Wang, J. Zhou, T. Koschny, and C. M. Soukoulis, *Appl. Phys. Lett.* **94**, 151112 (2009).
- [34] See Supplemental Material at <http://link.aps.org/supplemental/10.1103/PhysRevLett.122.203903> for more details.
- [35] M. I. Dyakonov, *Sov. Phys. JETP* **67**, 714 (1988).
- [36] B. Yang, M. Lawrence, W. Gao, Q. Guo, and S. Zhang, *Sci. Rep.* **6**, 21461 (2016).
- [37] C. Fang, H. Weng, X. Dai, and Z. Fang, *Chin. Phys. B* **25**, 117106 (2016).
- [38] B. Bradlyn, J. Cano, Z. Wang, M. G. Vergniory, C. Felser, R. J. Cava, and B. A. Bernevig, *Science* **353**, aaf5037 (2016).
- [39] J. Hou, Z. Li, X. W. Luo, Q. Gu, and C. Zhang, *arXiv:1808.06972*.
- [40] R.-P. Guo, Q.-H. Guo, L.-T. Wu, J. Chen, and D. Fan, *Opt. Express* **24**, 13788 (2016).
- [41] S. Jeon, B. B. Zhou, A. Gyenis, B. E. Feldman, I. Kimchi, A. C. Potter, Q. D. Gibson, R. J. Cava, A. Vishwanath, and A. Yazdani, *Nat. Mater.* **13**, 851 (2014).
- [42] H. Jia, R. Zhang, W. Gao, Q. Guo, B. Yang, J. Hu, Y. Bi, Y. Xiang, C. Liu, and S. Zhang, *Science* **363**, 148 (2019).
- [43] J. K. Gansel, M. Thiel, M. S. Rill, M. Decker, K. Bade, V. Saile, G. von Freymann, S. Linden, and M. Wegener, *Science* **325**, 1513 (2009).
- [44] T. Bückmann, N. Stenger, M. Kadic, J. Kaschke, A. Frölich, T. Kennerknecht, C. Eberl, M. Thiel, and M. Wegener, *Adv. Mater.* **24**, 2710 (2012).
- [45] H. O. T. Ware, A. C. Farsheed, B. Akar, C. Duan, X. Chen, G. Ameer, and C. Sun, *Mater. Today Chem.* **7**, 25 (2018).